RSC Advances

ROYAL SOCIETY OF CHEMISTRY

www.rsc.org/advances

Ag_2S sensitized mesoporous Bi_2WO_6 architectures with enhanced visible light photocatalytic activity and recycle properties.

Owais Mehraj[†], Bilal M. Pirzada[†], Niyaz A. Mir[††], Saima Sultana[†], Suhail Sabir[†]*,

[†]*Department of Chemistry, Aligarh Muslim University, Aligarh – 202002, India*

[††]*Solid State and Structural Chemistry Unit, Indian Institute of Science, Bangalore-560012, India*

***Corresponding Author:** Dr. Suhail Sabir, Department Of Chemistry, Aligarh Muslim University, Aligarh, India, 202002.

Email: *sabirsuhail09@gmail.com*

Phone: +91-571-2700920-ext-3366

Abstract

To harvest the solar energy more efficiently, novel Ag_2S/Bi_2WO_6 heterojunctions were synthesized by a hydrothermal route. This novel photocatalyst was synthesized by impregnating Ag_2S into Bi_2WO_6 semiconductor by hydrothermal route without any surfactants or templates. The as prepared structures were characterized by multiple techniques such as X-ray diffraction (XRD), X-ray photoelectron spectroscopy (XPS), Brunauer–Emmet–Teller (BET) analysis, scanning electron microscopy (SEM), transmission electron microscopy (TEM), energy dispersive X-ray spectrometry (EDS), UV-vis diffuse reflection spectroscopy (DRS) and photoluminescence (PL). The characterization results suggest the mesoporous hierarchical spherical structures with high surface area and improved photo response in the visible spectrum. Compared to the bare Bi_2WO_6, the Ag_2S/Bi_2WO_6 exhibited much higher photocatalytic activity towards the degradation of Rhodamine B (RhB). Although silver based catalysts are easily eroded by photogenerated holes, the Ag_2S/Bi_2WO_6 photocatalyst was found to be highly stable in the cyclic experiments. Based on the results of BET, Pl and DRS analysis, two possible reasons have been proposed for the enhanced visible light activity and stability of this novel photocatalyst: (1) broadening of photoabsorption range and (2) efficient separation of photoinduced charge carriers which does not allow the photoexcited electrons to accumulate on conduction band of Ag_2S and hence prevents the photocorrosion.

Keywords: Ag_2S/Bi_2WO_6 heterojunctions; Photoresponse; Mesoporous; Rhodamine B; visible light photocatalysis.

1. Introduction

The growing environment concerns and energy demand are the main driving forces for the sustained fundamental and applied research in the area of semiconductor photocatalysis for organic pollutant degradation and hydrogen generation from water splitting using solar light.[1-3] Semiconductor photocatalysis involves the photoinduced generation of electron –hole pairs, therefore an ideal photocatalyst should have extended spectral responsive range and low recombination rate of photogenerated charge carriers.[4] Coupling of two photocatalysts to form heterojunction may provide a chance to develop a new photocatalyst with enhanced separation of photoinduced charge carriers and extended photoabsorption range.[5,6]

Bi_2WO_6 is one of the simple Aurivillius Oxide with perovskite-like slabs of WO_4^{2-} and $Bi_2O_2^{2+}$.[7,8] Owing to its non-toxicity and strong oxidizing power, Bi_2WO_6 has been used as one of the promising and excellent photocatalyst for the decomposition of organic pollutants under visible light.[9-12] To improve the photocatalytic activity of bare Bi_2WO_6, many different morphologies of Bi_2WO_6 with different hierarchical architecture and surface area have been reported. These include the development of nanoplates,[13] porous thin films,[14] 3D nest like mesoporous Bi_2WO_6 architectures[15] and flower sphere like complex structures.[16,17] However there are still two important factors which limits the photocatalytic efficiency and thus hinders the practical application of bare Bi_2WO_6 (1) The absorption edge of pure Bi_2WO_6 is ca, 450 nm[18,19] which overlaps a small part of solar spectrum leading to the unsatisfactory photoresponse range (2) The recombination rate of photoinduced charge carriers is large and

therefore leads to the low quantum efficiency because of the short lifetimes of the electron hole pairs.[20,21]

Recent studies have shown that coupling of Bi_2WO_6 with other semiconductors improves the photocatalytic performance of Bi_2WO_6 to a substantial extent by promoting the effective separation of photoinduced charge carriers and broadening the visible light responsive range, For eg. α-Fe_2O_3/Bi_2WO_6,[22] Bi_2S_3/Bi_2WO_6,[4] Bi_2O_3 decorated Bi_2WO_6 and TiO_2 modified flower like Bi_2WO_6,[23] Bi_2WO_6/BiOBr,[24] WO_3–Bi_2WO_6[25] and CuPc sensitized Bi_2WO_6.[26]

As an important chalcogenide Ag_2S with a narrow band gap of 1.1 eV has been investigated extensively for the numerous applications such as photovoltaic device construction,[27,28] photocatalytic decomposition of organic pollutants[29,30] and photocatalytic H_2 production.[31] Moreover Ag_2S has high absorption coefficient[31-36] and besides Ag_2S is free from toxic heavy elements like Pb and Cd and thus possess negligible toxicity compared to other narrow band gap materials.[37] Owing to the high chemical stability, narrow band gap, high absorption coefficient and excellent optical limiting properties of Ag_2S, we choose to couple it with Bi_2WO_6 to form a heterojunction with enhanced visible light photocatalytic activity and high stability.

Herein for the first time we report novel Ag_2S/Bi_2WO_6 heterojunction photocatalyst to overcome the drawbacks of low photocatalytic efficiency of Bi_2WO_6 brought by narrow photoresponsive range and high rate of recombination of photoinduced charge carriers .The photocatalytic activity of the as prepared photocatalysts was evaluated by decomposing the dye Rhodamine B. The effect of Ag/Bi weight ratio on the photocatalytic activity was also studied. The stability of the catalyst which is a major concern for catalysts containing silver was also investigated.

2. Experimental

2.1. Synthesis of Ag_2S-Bi_2WO_6 photocatalyst

All the reagents were of analytical purity, purchased from Sigma-Aldrich India and used without further purification. The hierarchical structures of Ag_2S/Bi_2WO_6 were synthesized by a two-step process. In the first step the mesoporous Bi_2WO_6 microspheres were fabricated by a simple hydrothermal process via following procedure: 1 mmol of $Na_2WO_4.2H_2O$ was dissolved in 15 ml of ethylene glycol under constant stirring. Then 2 mmol of $Bi(NO_3)_3.5H_2O$ was added into the solution and the mixture was stirred for 20 min. Thereafter absolute ethanol (25 ml) was added into the solution and the suspension was transferred into a 50 ml Teflon-lined stainless steel autoclave and heated at 180 ^oC for 24h. The autoclave was subsequently cooled to room temperature and the products were collected by filtration. The as obtained products were washed with de-ionized water and absolute ethanol for several times and then dried at 80 ^oC for 12h.

In the second step, impregnation of Bi_2WO_6 surface with Ag_2S was carried out by *in-situ* growth of Ag_2S on Bi_2WO_6 substrate at room temperature. In a typical experimental procedure, 0.6 g of Bi_2WO_6 microspheres and different amounts of $AgNO_3$ were dispersed in 50 ml of absolute ethanol and ultrasonicated for 30 min. After ultrasonication, appropriate amount of Na_2S was added to the suspension with continuous stirring. The obtained suspension was vigorously stirred for 8 h. The precipitates were collected and washed with de-ionized water and absolute ethanol for several times and then dried at 80 ^oC for 12h. The different weight ratios of Ag_2S to Bi_2WO_6 samples were prepared and noted as 3% Ag_2S/Bi_2WO_6, 5% Ag_2S/Bi_2WO_6, 7% $Ag_2S/Bi2WO_6$ and 9% Ag_2S/Bi_2WO_6. For comparison pure Ag_2S was also synthesized in absence of Bi_2WO_6.

2.2. Characterization

To examine the phase purity and crystal structure of as prepared samples, XRD analysis was carried out using an PANalytical, XPert PRO powder X-ray diffractometer with CuKα radiation (λ= 1.5418 A°) having a tube voltage of 40kV and current of 30 mA at room temperature with the scan range 2θ = 15 to 80° and step size 0.02666°. X-ray photoelectron spectroscopy (XPS) was used to analyse the surface properties of samples using MK II photoelectron spectrometer having Al-K(alpha) (1486.6 eV) as the X-ray source. The particle morphology and microstructure of the samples was investigated by FESEM using Carl-Zeiss field-emission scanning electron microscope (FESEM) equipped with EDS attachment and transmission electron microscopy (TEM) using JEOL, JEM 2100F instrument. UV-vis DRS spectra of samples in the region of 300-800 nm was recorded by UV-vis NIR spectrometer (Perkin Elmer) equipped with an integrating sphere assembly. The surface area and pore size distribution of the as prepared samples was characterized by N_2 adsorption- desorption isotherm using Quantachrome Instruments Autosorb 1C. Adsorption of samples was done at 77 K and the samples were degased at 150 ^{o}C for 3 h before analysis. PL spectra was recorded on flourospectrometer.

2.3. Photocatalytic activity

To evaluate the photocatalytic activity of the samples, RhB and phenol aqueous solution was degraded under visible light irradiation. A 500 W, tungsten halogen lamp was used as the light source. Immersion well photoreactor made of pyrex glass was used to perform the experiments. Refrigerated circulating liquid bath was used to keep the temperature of the reaction constant at 20 ± 0.3 ^{0}C. The experiments were performed as follows. 0.18 g of the as prepared

catalyst was added into 180 mL RhB aqueous solution. Prior to the illumination, the suspension was magnetically stirred for at least 30 min in the dark to attain adsorption-desorption equilibrium between dye and catalyst. 5ml suspensions were sampled at 5 min

time intervals and centrifuged to remove the catalyst particles. The concentration of catalyst free dye solution was analysed at λ_{max} (554 nm) using Shimadzu UV–vis 1601, UV-vis spectrophotometer.

To determine the effect of scavengers on photocatalytic activity, appropriate quantity of scavenger species were introduced in the reaction system in a manner similar to photocatalytic experiment.

Photoluminescence (PL) technique with Terepthalic acid (TA) as a probe molecule was used for the detection of •OH radicals. The experimental procedure was referred to previous studies.[5]

3. Results and discussions

3.1. XRD analysis

XRD analysis was used to determine the purity, phase structure and crystallinity of the as prepared samples. Fig. 1 presents the XRD pattern of pristine Bi_2WO_6 and Ag_2S loaded Bi_2WO_6. As can be seen from the Fig. 1a, the diffraction peaks can be categorised into a set of 2θ at 28.3^o, 32.8^o, 47.1^o and 55.9^o corresponding to the indices (131), (200), (202) and (331) which indicates a perfectly orthorhombic structure for pure Bi_2WO_6.[38] Compared with diffraction pattern of bare Bi_2WO_6, no significant diffraction peaks of any other phase or impurity was observed on Ag_2S/Bi_2WO_6 composites indicating that the characteristic peaks associated with Ag_2S are not obviously detected (Fig. 1b-e). This may be due to the limited amount of Ag_2S (3% - 9%) used, small size of Ag_2S nanoparticles and high dispersion of Ag_2S on the surface of Bi_2WO_6 spherical architectures. More importantly the absence of individual Ag_2S aggregates in SEM images of as prepared samples indicate high dispersion of Ag_2S in composites. Fig. 1f displays the characteristic XRD pattern of pure Ag_2S sample. All peaks of pure Ag2S can be assigned to monoclinic Ag_2S crystal structure.[39] The average

crystallite size of the samples was calculated by using Scherer formula given below[5] and results are listed in table 1.

$$D = {k\lambda}/{\beta Cos\theta} \qquad (1)$$

where D is taken as crystallite size, k is a constant, λ is X-ray wavelength, β is the full width at half maximum (FWHM) measured in radians on the 2θ scale, θ is the Bragg angle for diffraction peaks. From the results of crystallite size displayed in table. 1, it is clear that there is negligible change in the crystallite size of pure Bi_2WO_6 and Ag_2S loaded Bi_2WO_6 samples.

3.2. XPX analysis

To further investigate the composition and oxidation states of as prepared samples, XPS analysis of 7% Ag_2S/Bi_2WO_6 heterostructure (Fig. 2) was carried out. Fig. 2a displays the overall XPX spectra for the 7% Ag_2S/Bi_2WO_6 in which peaks for Bi, W, O, Ag and S could be detected. The high resolution XPS spectra of Bi4f, W4f, O2S, S2p and Ag3d is shown in Fig. 2b-f. The Bi4f peaks (Fig. 2b) at 157.8 and 163.10 eV are attributed to the binding energies of $Bi4f_{7/2}$ and $Bi4f_{5/2}$ respectively which corresponds to previous results.[40] The W4f peaks at 34.00 and 36.1 eV are ascribed to binding energies of $4f_{7/2}$ and $4f_{5/2}$ (Fig. 2c).The splitting energy of 2.1 eV for 4f doublet of W indicates the +6 oxidation state of W in composite catalyst.[41] The O1S peak (Fig. 2d) at 528.8 eV is in good agreement with previous results.[40] The high resolution Ag3d XPS spectrum is displayed in Fig. 2e. The two peaks corresponding to Ag^+ at approximately 366.50 and 372.60 eV are attributed to the $Ag3d_{5/2}$ and $Ag3d_{3/2}$ respectively.[42] Since in previous results the peaks at 368.3 and 374.2 eV are attributed to metallic Ag whereas the peaks at 367.8 and 373.8 eV are attributed to Ag^+,[43,44] it implies that peaks obtained in our XPS results can be ascribed to Ag^+ only suggesting that no metallic Ag^0 is formed. Fig. 2f displays the S2P XPS spectrum. The peak at around 163 eV can be attributed to $S2P_{1/2}$ indicating the presence of S^{2-} which further suggests the formation

of Ag_2S.[45] From these results it can be confirmed that Ag_2S/Bi_2WO_6 composites have been successfully synthesized.

3.3. SEM, EDS and TEM analysis

To investigate the surface morphology of as prepared samples SEM characterization was used. Fig. 3 presents the FESEM images of pure Bi_2WO_6 and 7% Ag_2S/Bi_2WO_6 composite. As clear from the Fig. 3a, the FESEM image of bare Bi_2WO_6 consist of abundant hierarchically structured architectures of Bi_2WO_6 microspheres. The higher magnification (Fig. 3b) reveals that Bi_2WO_6 architectures are built from numerous nanoplates aligned to the spherical surface forming a microsphere. Compared with bare Bi_2WO_6 the Ag_2S loading affects the surface morphology of Bi_2WO_6 in composite (Fig. 3c) to some extent. As can be seen clearly from the higher magnification FESEM image of 7% Ag_2S/Bi_2WO_6 composite (Fig. 3d), it is somewhat different from spherical structure showing that Ag2S has combined well with Bi_2WO_6 to form a heterostructure. EDX spectrum of Bi_2WO_6 and 7% Ag_2S/Bi_2WO_6 was collected to confirm the presence of Ag_2S in hybrids. The EDS spectrum in Fig. 3e shows clearly that bare Bi_2WO_6 is composed of Bi, W and O elements while as Ag_2S/Bi_2WO_6 (Fig. 3f) composite is composed of Bi, W, O, Ag and S elements indicating the formation of Ag_2S/Bi_2WO_6 composite. To further confirm the high dispersion of Ag_2S in composite, EDX elemental mapping of 7 % Ag_2S/Bi_2WO_6 composite was performed as shown in Fig. 4. It can be seen from the Fig.4, that Ag (Fig. 4b) and S (Fig. 4e) are highly dispersed in 7% Ag_2S/Bi_2WO_6 hybrid.

TEM analysis was further used to investigate the detailed structure as shown in Fig. 5. It can be seen that Bi_2WO_6 structures are composed of nanoplates with a thickness around 10-20 nm (Fig. 5a). Fig. 5b shows that Bi_2WO_6 microspheres are mesoporous in nature which helps the

Ag_2S particles to bind in this composite system. The TEM image for 7% Ag_2S /Bi_2WO_6 (Fig. 5e-f) shows subtle particles of Ag_2S grown on the surface of Bi_2WO_6 microsphere. The presence of lattice fringes (Fig. 5c) confirms the crystalline nature of Bi_2WO_6. Furthermore the spacing of lattice fringes was found to be 0.313 nm which corresponds to the 131 planes of orthorhombic Bi_2WO_6.[38] The SAED (Selected Area Diffraction Pattern) demonstrates the presence of clear diffraction spots (Fig. 5d) which further confirms the crystalline structure of Bi_2WO_6. All these above results are in good agreement with the results of XRD and XPS analyses and strongly demonstrate the formation of Ag_2S/Bi_2WO_6 heterojunction.

3.4. N_2 Adsorption-Desorption

Fig. 6 shows the nitrogen adsorption isotherm and pore size distribution of pure Bi_2WO_6 (Fig. 6a) and 7% Ag_2S/Bi_2WO_6 (Fig. 6b). As can be seen from the figure, the shape of both the isotherms seem to be nearly of type IV isotherm with hysteresis loop at higher relative pressure which is usually associated with capillary condensation in mesopores.[46,47] The type H3 hysteresis loop at higher relative pressure according to IUPAC classification reflect the presence of slit like pores indicating the presence of mesopores in the region of 2-10 nm which is further confirmed by the BJH pore size distribution diagram in the inset of Fig. 6. The BET surface area of bare Bi_2WO_6 and 7% Ag_2S/Bi_2WO_6 are 77.6 m^2g^{-1} and 66 m^2g^{-1} respectively indicating that the loading of Ag_2S leads to the decrease in surface area to some extent which is probably because Ag_2S particles are embedded in the pores of Bi_2WO_6.[48] The presence of mesoporous structure with large surface area provides more active sites and transport paths for the decomposition of contaminants in photocatalytic reaction.

3.5. Optical properties

Fig. 7 displays the UV-vis diffuse reflectance (DRS) spectra of bare Bi_2WO_6 and Ag_2S/Bi_2WO_6 heterostructures. As shown in Fig.7a the bare Bi_2WO_6 has an absorption edge

around 450 nm, where as weak and broadened peaks of Ag_2S (Fig. 7b) are similar to the reported UV-vis spectra of pure Ag_2S.[48,49] With increase in Ag_2S loading the absorption edge of heterostructure samples is shifted to longer wavelengths from 450-490 nm.

The optical band gaps (insets of Fig. 7a and 7b) of Bi_2WO_6 and Ag_2S were calculated using the equation reported by Butler.[50]

$$h\nu \times \alpha = (Ah\nu - E_g)^{n/2} \quad (2)$$

Since α is proportional to Kubelka - Munk Function F(R), the equation becomes

$$h\nu \times F(R) = (Ah\nu - E_g)^{n/2} \quad (3)$$

Where, h is the planks constant, ν is the frequency, A is the proportionality constant and E_g is the band gap energy. The value of n is determined by the type of transition (n = 1 for direct and n = 4 for indirect transition). The n for Bi_2WO_6 has been reported by some researchers as 1 (direct transition),[51,52] and by some other researchers as 4 (indirect transition).[53,54] In our case we plotted $(F(R) \times h\nu)^{1/2}$ versus $h\nu$ for Bi_2WO_6 (inset of Fig. 7a) and $(F(R) \times h\nu)^2$ versus $h\nu$ for Ag_2S (inset of Fig. 7b). The band gaps for Bi_2WO_6 and Ag_2S were estimated as 2.74 eV and 1.1 eV respectively.

3.6. Photocatalytic properties

To assess the photocatalytic activity of as prepared samples, RhB was selected as a probe molecule. The characteristic absorption band of RhB at 554 nm was employed to determine the process of degradation. Fig. 8 displays the photocatalytic performances of all Ag_2S/Bi_2WO_6 heterojunctions with different Ag_2S contents over degradation of RhB (C_t/C_0) under visible light irradiation. As shown in Fig. 8b, the blank experiment (without photocatalyst) shows that the concentration of RhB remains unchanged even after 50 min of visible light irradiation indicating the significance of photocatalyst. The adsorption of RhB

dye by 7% $Ag_2S/Bi2WO_6$ was also checked for 50 min and it was found that the adsorption in dark is insignificant. As is shown the pure mesoporous Bi_2WO_6 exhibit photocatalytic efficiency of 56.5 % in 50 min. The better performance of pure mesoporous Bi_2WO_6 photocatalyst was attributed to the high surface area and mesoporous structure of Bi_2WO_6. The high surface area and mesoporous structure not only provide more active sites and transport paths in photocatalytic reaction but also improves the contact of photocatalyst with organic pollutants. When Ag_2S and Bi_2WO_6 are combined to construct a heterostructure, the photocatalytic activity of the composites is dramatically enhanced even though the Ag_2S content is very low. The photocatalytic activity of all Ag_2S/Bi_2WO_6 heterostructures with Ag_2S weight percentage of 3 %, 5%, 7% and 9% is higher than the bare Bi_2WO_6 and are listed in table 1. The best photocatalytic performance was obtained for 7 % Ag_2S/Bi_2WO_6 for which almost 85% of RhB was degraded in 50 min. The reason for enhanced visible light activity is the formation of heterojunction which results into the generation of natural energy bias at heterojunction with subsequent transfer of photoinduced charge carriers and thereby impeding the electron hole recombination, which is the main factor responsible for low visible light activity of Bi_2WO_6. With further increase in Ag_2S content to 9%, the photocatalytic activity decreases but is still higher than bare Bi_2WO_6. Therefore the optimal content of Ag_2S in Ag_2S/Bi_2WO_6 composite is 7 %. The optimum content of AgBr in the heterojunction can be related to two factors. (1) For efficient electron–hole separation the space charge region potential must be certain.[38] When Ag_2S content was above 7% (optimal value) the space charge region might become narrow and lead to the recombination of photoinduced charge carriers. (2) The loading of Ag_2S leads to decrease in surface area as discussed in section 3.4. When Ag2S content was above optimal value the surface area might decrease substantially leading to decrease in photocatalytic activity. Fig. 8a displays the absorption spectral changes of the photocatalytic degradation of RhB aqueous solution over

7% Ag_2S/Bi_2WO_6. As can be seen from the Fig. 8a, the absorbance of RhB at 554 nm decreases significantly with increase in reaction time accompanied by a slight shift of absorption band towards blue region which is attributed to the step wise de-ethylation process of RhB into intermediates as reported in previous works.[55,56] The apparent pseudo first order kinetics model given by the equation (4) was applied in experiments to understand the reaction mechanism.[57]

$$\ln(C_0/C_t) = K_{app}t \qquad (4)$$

K_{app} is apparent pseudo-first order reaction constant and its value for bare Bi_2WO_6 and all heterojunctions was calculated via the first order linear fit data (Fig. 8c) and are displayed in table 1. From table I, it is clear that photocatalytic activity of 7%Ag_2S/Bi_2WO_6 is 2.4 times higher than the bare Bi_2WO_6 suggesting that Ag_2S/Bi_2WO_6 is an excellent photocatalyst under visible light.

3.7. Proposed Mechanism

The trapping experiments of active species formed during photocatalytic oxidation process were carried out to investigate the possible mechanism involved in RhB degradation over 7% Ag_2S/Bi_2WO_6 heterojunction. Benzoquinone (BQ)[58,59] isopropyl alcohol (IPA)[58,60] and ammonium oxalate (AO)[61] were used as superoxide ($^{\bullet}O_2^-$), hydroxyl ($^{\bullet}OH$) and hole (h^+) scavengers respectively. Fig. 9 displays the effect of different scavengers and it can be seen from the figure that the rate of RhB degradation decreases substantially in presence of AO. However addition of IPA had no obvious effect on Rate of RhB degradation whereas addition of BQ slightly decreases the photocatalytic performance of 7%Ag_2S/Bi_2WO_6 compared with no scavenger under same conditions. These results indicate that h^+ are the main active species rather than $^{\bullet}O_2^-$ and $^{\bullet}OH$ in the RhB degradation over 7%Ag_2S/Bi_2WO_6 system under visible light irradiation.

To further confirm that $^{\bullet}OH$ did not play any role, we carried out the Terepthalic acid photoluminescence studies. The PL spectral changes observed during irradiation of Ag_2S/Bi_2WO_6 in a basic terepthalic acid solution (315 excitation wavelength) are displayed in Fig. 10. As clear from the figure no Pl signals were observed at 425nm throughout the photocatalytic oxidation process, indicating that no $^{\bullet}OH$ is formed on the surface of catalyst.

To ensure that the reactive species originate from the photocatalytic process of catalysts and not form the sensitization of dye, we selected a colourless molecule phenol as a probe. Fig. 9b displays the photocatalytic performances of pure Bi_2WO_6 and 7% Ag_2S/Bi_2WO_6 heterojunctions over degradation of phenol (C_t/C_0) under visible light irradiation. As can be seen from the Fig. 9b the concentration of phenol decreases with increasing reaction time in presence of both pure Bi_2WO_6 and 7% Ag_2S/Bi_2WO_6. The concentration (C_t/C_0) decreases sharply in presence of 7% Ag_2S/Bi_2WO_6 under visible light irradiation while as in case of pure Bi_2WO_6 the decrease in the concentration (C_t/C_0) of phenol is lower than 7% Ag_2S/Bi_2WO_6. Since phenol cannot absorb visible light, it follows directly that reactive spies originate from the photocatalytic process of samples under visible light ruling out the possibility of sensitization of dye. The results obtained are in accordance with the results obtained for the degradation of RhB.

The BET surface area of bare Bi_2WO_6 was calculated to be 77.6 m^2g^{-1}. The high surface area and mesoporous structure of Bi_2WO_6 makes it an excellent visible light photocatalyst but the surface area of 7% Ag_2S/Bi_2WO_6 was calculated to be only 66 m^2g^{-1} which is obviously less than the bare Bi_2WO_6. The Ag_2S loading on the surface of Bi_2WO_6 enhances the visible light photocatalytic activity of Bi_2WO_6 substantially although the surface area is decreased. Therefore it can be assumed that large surface area may be responsible for the high photocatalytic activity of bare Bi_2WO_6 but it is not the influence factor for the enhancement of visible light activity of Ag_2S/Bi_2WO_6 composites up to 7% loading. Therefore to analyse

the mechanism of improved photocatalytic activity of Ag_2S/Bi_2WO_6 composites the relative positions of the conduction band and valence band edges of Ag_2S and Bi_2WO_6 were investigated for the flow chart of photoinduced charge carriers in a heterojunction. The relative position of valence band (VB) of Ag_2S and Bi_2WO_6 was evaluated by the empirical formula in equation (5).[62]

$$E_{VB} = X - E^c + 0.5E_g \quad (5)$$

Where X is the electronegativity of semiconductor expressed as geometric mean of absolute electronegativity of constituent atoms, E^c is the energy of free electrons on hydrogen scale (4.5 eV) and E_g is the band gap energy. The E_{VB} for Ag_2S and Bi_2WO_6 were calculated to be 1.1 eV and 3.23 eV respectively. The relative position of conduction band (CB) of Ag_2S and Bi_2WO_6 were estimated from equation (6).

$$E_{CB} = E_{VB} - E_g \quad (6)$$

The E_{CB} for Ag_2S and Bi_2WO_6 were calculated to be 0 eV and 0.49 eV respectively.

Based on the results of BET analysis, DRS, Trapping experiments and TA PL spectra we presented a schematic diagram (Fig. 11) to illustrate the photocatalytic reaction mechanism and charge transfer of Ag_2S/Bi_2WO_6 system. We propose that under visible light irradiation both Ag_2S and Bi_2WO_6 are excited and generate electron hole pairs. Since the CB energy level of Ag_2S and Bi_2WO_6 is 0 and 0.49 eV (Vs SHE), the single electron reduction of O_2 to $^{\bullet}O_2^-$(-0.046 vs SHE) [63,64] is not possible .When two semiconductors are in contact, the electrons from less positive conduction band of Ag_2S (0 eV) are injected with high efficiency into more positive conduction band of Bi_2WO_6 (0.49 ev). On the other hand holes from more positive valence band of Bi_2WO_6 (3.23 eV) are transferred to the less positive VB of Ag_2S (1.1 eV). The photoinduced charge carriers are thus effectively separated at the interface of Ag_2S/Bi_2WO_6. The holes (h^+) on the valence band of Ag_2S could not react with OH^-/H_2O to

form $^{\bullet}OH$ because VB of Ag_2S is more negative (1.1 eV) than that of $^{\bullet}OH/H_2O$ (2.30 eV vs SHE).[38] Hence holes from valence band of Ag_2S migrate to the surface of a photocatalyst where they take part in photocatalytic reaction to mineralize the organic pollutants and thereby enhancing the photocatalytic activity.

Photoluminescence spectra of hierarchically structured bare Bi_2WO6 and 7% $Ag2S/Bi_2WO_6$ was carried out to further demonstrate the enhancement of separation of charge carriers. The lower intensity of PL peak represents the lower probability of electron-hole recombination. Fig.12 presents the PL spectra of bare Bi_2WO_6 and 7%Ag_2S/Bi_2WO_6 with an excitation wavelength of 380 nm. From the Fig.12 it is clear that the intensity of PL spectra decreases significantly in 7% Ag_2S/Bi_2WO_6 compared to the bare Bi_2WO_6 indicating that the loading of Ag_2S on Bi_2WO_6 has greatly restrained the recombination of photoinduced charge carriers between Bi 6S and O 2P to the empty W4d orbitals.[22]

3.8. Stability of the Catalyst and cycling runs.

The stability of silver based compounds has always been a matter of concern,[65] particularly the metal chalcogenides get easily eroded by the photogenerated holes.[66] Therefore cyclic experiments with 7% Ag_2S/Bi_2WO_6 sample were carried out to determine the stability of a photocatalyst. Fig. 13 displays the results of RhB degradation by 7%Ag_2S/Bi_2WO_6 after 4 repeated cycles. It can be seen from the Fig. 13 that the degradation of RhB by 7% Ag_2S/Bi_2WO_6 is maintained at 81.3 % even after 4 repeated cycles indicating the high stability of photocatalyst. Fig.14 presents the Ag3d XPS spectrum and XRD analysis of used 7% Ag_2S/Bi_2WO_6 catalyst after 4 repeated cycles. It is clear from the Fig. 14a that the Ag3d XPS spectrum of used catalyst is similar to that of fresh catalyst (Fig. 2e) with no peak detected for metallic Ag in used catalyst after 4 repeated cycles. The XRD analysis of used catalyst (Fig. 14b) after 4 repeated cycles also confirms that the structure and phase of the used catalyst remains intact with no additional peak detected for Ag metal. From these results

it is clear that the Ag_2S/Bi_2WO_6 is a stable photocatalyst under visible light irradiation and the main reason for the enhanced stability is the transfer of CB electrons from Ag_2S to Bi_2WO_6 which reduces the chances of erosion of catalyst.

3.9. Conclusion

Mesoporous Bi_2WO_6 was modified with Ag_2S by hydrothermal method without any surfactant or template. The introduction of Ag_2S extended the photoabsorption range of Bi_2WO_6 and the composite showed red shift compared to the pure Bi_2WO_6. The Ag_2S/Bi_2WO_6 heterostructures showed enhanced photocatalytic activity in the degradation of RhB under visible light irradiation which is 2.4 times higher than the pure Bi_2WO_6. The Ag_2S/Bi_2WO_6 composite even after 4 recycling runs did not show any significant decrease in photocatalytic activity except for about 4%. The enhanced photocatalytic activity and stability was attributed to the broadening of photoabsorption range and efficient separation of the photoinduced electron hole pairs as a result of natural energy bias at heterojunction. This study inspires a thought of utilizing visible spectrum efficiently and simultaneously presents a way to promote separation of photo induced electron hole pairs.

Acknowledgements

The authors are highly thankful to Department of Physics AMU Aligarh, USIF AMU Aligarh and Department of Chemistry AMU Aligarh for providing the instrumentation facility. DST and UGC is duly acknowledged for financial support in the form of FIST, PURSE and DRS II research grants .The authors are also thankful to UGC, New Delhi, India for providing financial assistance. Niyaz A. Mir thanks Department of Science & Technology, India for the award of Young Scientist grant (SERB/F/1214/2014-2015).

References

1. Z. G. Zou, J. H.Ye, K. Sayama and H. Arakawa, *Nature*, 2001, **414**, 625−627.

2. N. Z. Bao, L. M. Shen, T. Takata and K. Domen, *Chem. Mater*., 2008, **20**, 110−117.
3. W. Morales, M. Cason, O. Aina, N. R. Tacconi and K. Rajeshwar, *J. Am. Chem. Soc*., 2008, **130**, 6318−6319.
4. (a) Z. Zhang, W. Wang, L.Wang and S. Sun, *Appl. Mater. Interfaces,* 2012, **4**, 593−597, (b) S. Sultana, Rafiuddin, M. Z. Khan, M. Shahadat, *J. Environ. Chem. Eng*., 2015,
5. J. Cao, B. Xu, H. Lin, B. Luo, S. Chen, *Chem. Eng. J*., 2012, **185–186**, 91–99.
6. Y. F. Hou, S. J. Liu, J. H. Zhang, X. Cheng and Y. Wang, *Dalton Trans*., 2014, **43**, 1025–1031.
7. S. S. Yao, J. Y. Wei, B. B. Huang, S. Y. Feng, X. Y. Zhang, X.Y. Qin, P. Wang, Z. Y. Wang, Q. Zhang, X. Y. Jing and J. Zhan, *J. Solid State Chem*., 2009, **182**, 236.
8. Y. F. Sun, Y. Xie, C. Z. Wu, S. D. Zhang and S. S. Jiang, *Nano Res*., 2010, **3**, 620.
9. L. S. Zhang, H. L. Wang, Z. G. Chen, P. K. Wong and J.S. Liu, *Appl. Catal*. B, 2011, **106**, 1-13.
10. H. F. Cheng, B. B. Huang, Y. Dai, X. Y. Qin, X. Y. Zhang, Z. Y. Wang and M. H. Jiang, *J. Solid State Chem*., 2009, **182**, 2274.
11. F. Amano, A. Yamakata, K. Nogami, M. Osawa and B. Ohtani, *J. Am. Chem. Soc*., 2008, **130**, 17650–17651.
12. G. S. Li, D. Q. Zhang, J. C. Yu and M. K. H. Leung, *Environ. Sci. Technol*., 2010, **44**, 4276–4281.
13. C. Zhang and Y. F. Zhu, *Chem. Mater*., 2005, **17**, 3537–3545.
14. L. W. Zhang, Y. J. Wang, H. Y. Cheng, W. Q. Yao and Y. F. Zhu, *Adv. Mater*., 2009, **21**, 1286–1290.
15. D. J. Wang, Y. Z. Zhen, G. L. Xue, F. Fu, X. M. Liu and D. S. Li, *J. Mater. Chem. C*, 2013, **1**, 4153.

16. L. Zhang, W. Wang, Z. Chen, L. Zhou, H. Xu and W. Zhu, *J. Mater. Chem*., 2007, **17**, 2526.

17. F. Amano, K. Nogami, R. Abe and B. Ohtani, *Chem. Lett*., 2007, **36**, 1314–1315.

18. L. Wu, J. H. Bi, Z. H. Li, X. X. Wang and X. Z. Fu, *Catal. Today*, 2008, **131**, 15.

19. Z. J. Zhang, W. Z. Wang, M. Shang and W. Z. Yin, *J. Hazard. Mater*., 2010, **177**, 1013.

20. S. Shamaila, A. K. Leghari Sajjad, F. Chen and J. L. Zhang, *Appl. Catal*. *B*, 2010, **94**, 272.

21. J. Ren, W. Z. Wang, S. M. Sun, L. Zhang and J. Chang, *Appl. Catal*. *B*, 2009, **92**, 50.

22. Y. Guo, G. Zhang, J. Liua and Y. Zhang, *RSC Adv*., 2013, **3**, 2963–2970.

23. (a) H. Wang, S. Li, L. Zhang, Z. Chen, J. Hu, R. Zou, K. Xu, G. Song, H. Zhao, J. Yangc and J. Liu, *CrystEngComm*, 2013, **15**, 9011–9019, (b) Y. Zheng, K. Lv, X. Li, K. Deng, J. Sun, L. Chen, L. Cui, *Chem. Eng. Technol.,* 2011, **34**, 1630-1634.

24. J.Xia, J. Di, S. Yin, H. Xu, J. Zhang, Y. Xu, L.Xu, H. Li and M.Jia, *RSC Adv*., 2014, **4**, 82–90

25. Y. Peng, Q. G. Chen, D. Wang, H. Y. Zhoua and A. W. Xu, *CrystEngComm*, 2015, **17**, 569–576.

26. Z. Zhang, W. Wang and L. Zhang, *Dalton Trans*., 2013, **42**, 4579–4585.

27. A. Tubtimtae, K.-L. Wu, H.-Y. Tung, M.-W. Lee and G. J. Wang, *Electrochem. Commun*., 2010, **12**, 1158.

28. J.-J. Wu, R.-C. Chang, D.-W. Chen and C.-T. Wu, *Nanoscale*, 2012, **4**, 1368.

29. Z.D. Meng, T. Ghosh, L. Zhu, J.G. Choi, C.Y. Park, W.C. Oh, *J. Mater. Chem*., 2012, **22,** 16127–16135.

30. X. Yi, H. S. Hwan, K. Y. Nam, Y. S. Hwa, C. S. Oh, *Nanotechnology*, 2010, **21**, 015703.

31. K. Nagasuna, T. Akita, M. Fujishima, H. Tada, *Langmuir*, 2011, **27**, 7294–7300.

32. I. Hwang and K. Yong, *ChemPhysChem*, 2013, **14**, 364.

33. Y. X. Li, G. Chen, C. Zhou and J. X. Sun, *Chem. Commun*., 2009, 2020.

34. R. Vogel, P. Hoyer and H. Weller, *J. Phys. Chem*., 1994, **98**, 3183.

35. S. Liu, X. T. Wang, W. X. Zhao, K. Wang, H. X. Sang and Z. He, *J. Alloys Compd*., 2013, **568**, 84.

36. S. H. Shen, L. J. Guo, X. B. Chen, F. Ren and S. S. Mao, *Int. J. Hydrogen Energy*, 2010, **35**, 7110.

37. Y. P. Du, B. Xu, T. Fu, M. Cai, F. Li, Y. Zhang and Q. B. Wang, *J. Am. Chem. Soc*., 2010, **132**, 1470.

38. D. Wang, L. Guo, Y. Zhen, L. Yue, G. Xue and F. Fu, *J. Mater. Chem. A*, 2014, **2**, 11716–11727.

39. X. Wang, S. Zhan, Y. Wang, P. Wang, H. Yu, J. Yu, C. Hu, *J. Colloid Interface Sci*., 2014, **422**, 30–37.

40. J. Wu, F. Duan, Y. Zheng and Y. Xie, *J. Phys. Chem. C*, 2007, **111**, 12866.

41. M. Penza, M. A. Tagliente, L. Mirenghi, C. Gerardi, C. Martucci and G. Cassano, *Sens. Actuators, B*, 1998, **50**, 9–18.

42. S. Bai, X. P. Shen, H. W. Lv, G. X. Zhu,C. L. Bao and Y. X. Shan, *J. Colloid Interface Sci*., 2013, **405**, 1–9.

43. M. Pang, J.Hu and H. C. Zeng, *J. Am. Chem. Soc.,* 2010, **132**, 10771.

44. H. Zhang, G. Wang, D. Chen, X. Lv and *J. Li, Chem. Mater*., 2008, **20**, 6543.

45. L. Qi, J. Yu, M. Jaroniec, *Phys. Chem. Chem. Phys*., 2011, **13,** 8915–8923.

46. H. G. Yu, R. Liu, X. F. Wang, P. Wang and J. G. Yu, *Appl. Catal. B*, 2012, **111–112**, 326.

47. G. I. N. Waterhouse, G. A. Bowmaker and J. B. Metson, *Phys. Chem. Chem. Phys.,* 2001, **3**, 3838.

48. D. Jiang, L. Chen, J. Xie and M. Chen, *Dalton Trans.,* 2014, **43**, 4878–4885.

49. J. P. Xiao, Y. Xie, R. Tang and W. Luo, *J. Mater. Chem.*, 2002, **12**, 1148.

50. M.A. Butler, *J. Appl. Phys*., 1977, **48**, 1914–1920.

51. G. Zhao, S. Liu, Q. Lu, F. Xu, H. Sun, *J. Alloys Compd*., 2013, **578**, 12–16.

52. C. Bhattacharya, H.C. Lee, A.J. Bard, *J. Phys. Chem. C*, 2013, **117**, 9633–9640.

53. F. Amano, K. Nogami, B. Ohtani, *Catal. Commun*., 2012, **20,** 12–16.

54. H. Fu, S. Zhang, T. Xu, Y. Zhu, J. Chen, *Environ. Sci. Technol.,* 2008, **42**, 2085–2091.

55. J. Fu, Y. L. Tian, B. B. Chang, F. N. Xi and X. P. Dong, *J. Mater. Chem.*, 2012, **22**, 21159.

56. J. X. Xia, S. Yin, H. M. Li, H. Xu, L. Xu and Y. G. Xu, *Dalton Trans*., 2011, **40**, 5249.

57. C.-H. Wu, H.-W. Chang, J.-M. Chern, *J. Hazard. Mater*., 2006**, 137,** 336-343.

58. G.T. Li, K.H. Wong, X.W. Zhang, C. Hu, J.C. Yu, R.C.Y. Chan, P.K. Wong, *Chemosphere,* 2009, **76**, 1185–1191.

59. M.C. Yin, Z.S. Li, J.H. Kou, Z.G. Zou, *Environ. Sci. Technol*. 2009, **43**, 8361–8366.

60. L.S. Zhang, K.H. Wong, H.Y. Yip, C. Hu, J.C. Yu, C.Y. Chan, P.K. Wong, *Environ. Sci. Technol.*, 2010, **44**, 1392–1398.

61. N. Zhang, S.Q. Liu, X.Z. Fu, Y.J. Xu, *J. Phys. Chem. C*, 2011, **115**, 9136–9145.

62. X. Zhang, L.Z. Zhang, T.F. Xie, D.J. Wang, *J. Phys. Chem. C*, 2009, **113**, 7371–7378.

63. X. Wang, S. Li, Y. Ma, H. Yu, J. Yu, *J. Phys. Chem. C*, 2011, 115, 14648–14655.

64. A.J. Bard, R. Parsons, J. Jordan, *Standard Potentials in Aqueous Solutions*, *CRC Press, New York*, 1985.

65. O. Mehraj, N. A. Mir, B. M. Pirzada, S. Sabir, M. Muneer J. Mol. Cat. A Chem., 2014, **395** 16–24

66. J. Ran, J. Yu, M. Jaroniec, Green Chem.2011, **13**, 2708–2713.

Figure Captions

Fig. 1 XRD patterns of (a) the pure Bi_2WO_6, (b) the 3% Ag_2S/Bi_2WO_6 catalyst, (c) the 5% Ag_2S/Bi_2WO_6 catalyst, (d) the 7% Ag_2S/Bi_2WO_6 catalyst, (e) the 9% Ag_2S/Bi_2WO_6 catalyst, and (f) the pure Ag_2S.

Fig. 2 XPS spectra of 7% Ag_2S/Bi_2WO_6. (a) Full survey spectra, and the high resolution XPS spectra of the sample: (b) Bi 4f, (c) W 4f, (d) O 1s, (e) Ag 3d, and (f) S 2p.

Fig. 3 FE-SEM images of samples. (a) Pure-Bi_2WO_6, (b) the high magnification SEM image of Pure-Bi_2WO_6, (c) 7% Ag_2S/Bi_2WO_6, (d) the high magnification SEM image of 7% Ag_2S/Bi_2WO_6, (e) EDS spectrum of Pure-Bi_2WO_6 sample, and (f) EDS spectrum of 7% Ag_2S/Bi_2WO_6 sample.

Fig. 4 EDS elemental mapping of 7% Ag_2S/Bi_2WO_6.

Fig. 5 TEM images of samples. (a and b) Pure Bi_2WO_6, (c and d) SAED pattern of Pure Bi_2WO_6, and (e and f) 7% Ag_2S/Bi_2WO_6

Fig. 6 N_2 adsorption–desorption isotherm of the samples. (a) Pure Bi_2WO_6, and (b) 7% Ag_2S/Bi_2WO_6. The inserts are the pore size distribution of the respective catalysts.

Fig. 7 UV–Vis diffuse reflectance spectra of (a) the pure Bi_2WO_6, and Ag_2S/Bi_2WO_6 composites (b) the pure Ag_2S catalyst. The insets in the (Fig. 7a and 7b) are band gap energies of the pure Bi_2WO_6, and Pure Ag_2S respectively.

Fig. 8 (a) UV–Vis spectral changes of the degradation of RhB by the 7% Ag_2S/Bi_2WO_6 catalyst, (b) the degradation efficiency (C_t/C_0) of RhB in presence of pure Bi_2WO_6 and Ag_2S/Bi_2WO_6 composites with different Ag_2S contents and (c) Rhodamine B decolourization curves of $\ln(C_0/C_t)$ versus irradiation time for different catalysts.

Fig. 9 (a) Effect of different scavengers on the degradation of RhB over 7% Ag_2S/Bi_2WO_6 catalyst; BQ = benzoquinone, IA = Isopropyl alcohol, AO = ammonium oxalate. (b) the degradation efficiency (C_t/C_0) of phenol in presence of pure Bi_2WO_6 and 7 % Ag_2S/Bi_2WO_6 composite.

Fig. 10 •OH trapping PL spectral changes over 7% Ag_2S/Bi_2WO_6 catalyst in a basic terepthalic acid solution (excitation at 315 nm) with irradiation time.

Fig. 11 Schematic diagram showing the band structure and separation of photoinduced electron hole pairs at interface of 7% Ag_2S/Bi_2WO_6 catalyst under visible light irradiation.

Fig. 12 PL spectra of samples. (a) Pure-Bi_2WO_6 and (b) 7% Ag_2S/Bi_2WO_6 (E_x = 380 nm).

Fig. 13 The repeated experiments of photocatalytic degradation of RhB over 7% Ag_2S/Bi_2WO_6 catalyst.

Fig.14 (a) Ag 3d XPS spectra of used 7% Ag_2S/Bi_2WO_6 catalyst after 4 recycling runs, and (b) XRD pattern of used 7% Ag_2S/Bi_2WO_6 catalyst after 4 recycling runs.

Table. 1 Pseudo-first-order rate constants (k_{app}) calculated from the plots of ln (C_0/C_t) versus irradiation time for decolorization of RhB over different catalysts, % decolorization of RhB and average crystallite size of Pure Bi_2WO_6 and Ag_2S/Bi_2WO_6 catalysts with different Ag_2S contents.

Fig.1

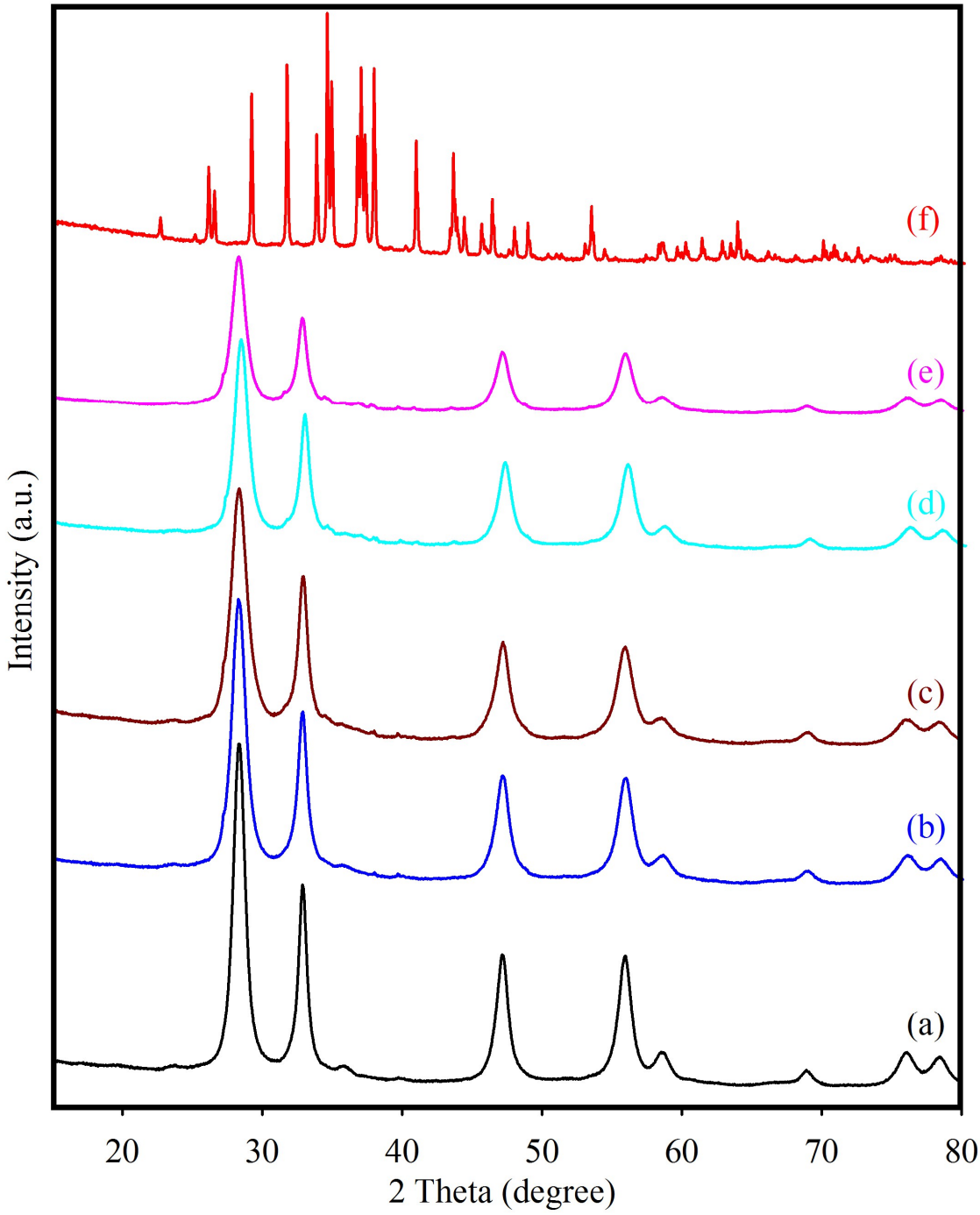

Fig.2

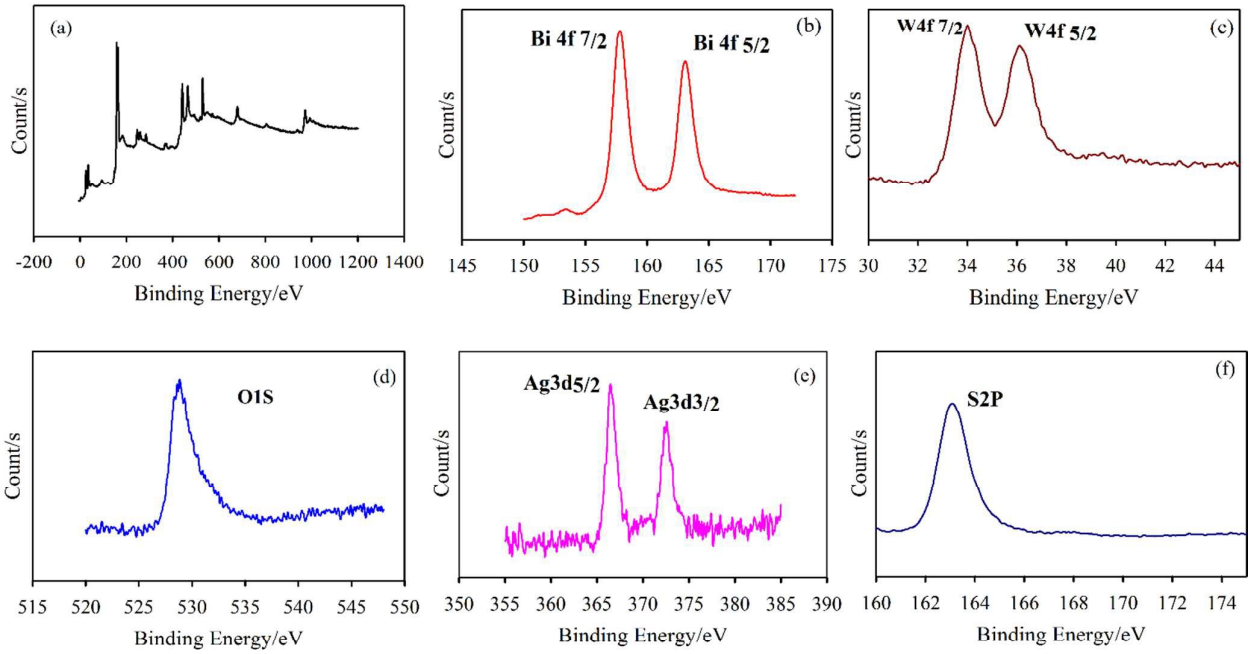

Fig.3

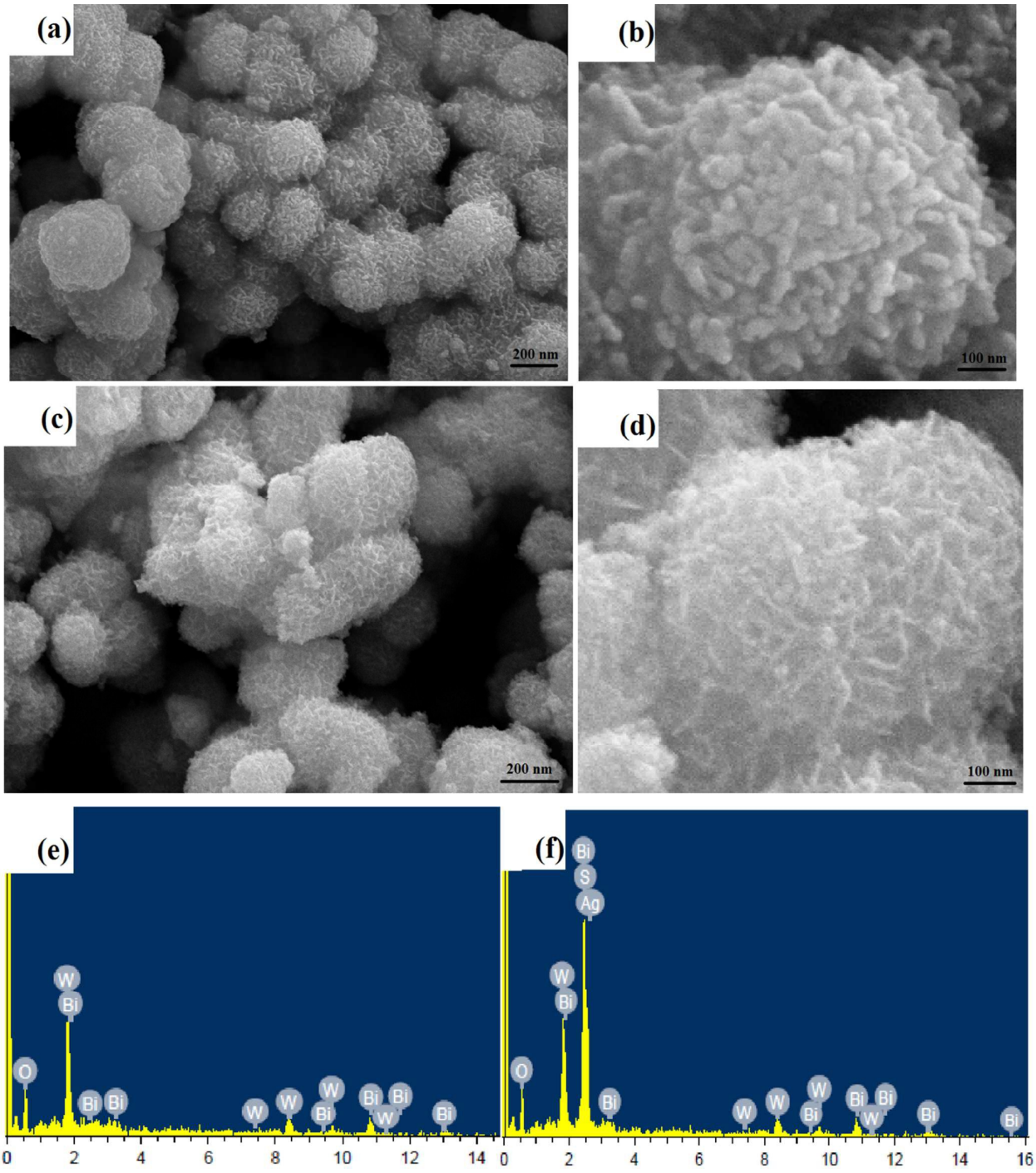

Fig.4

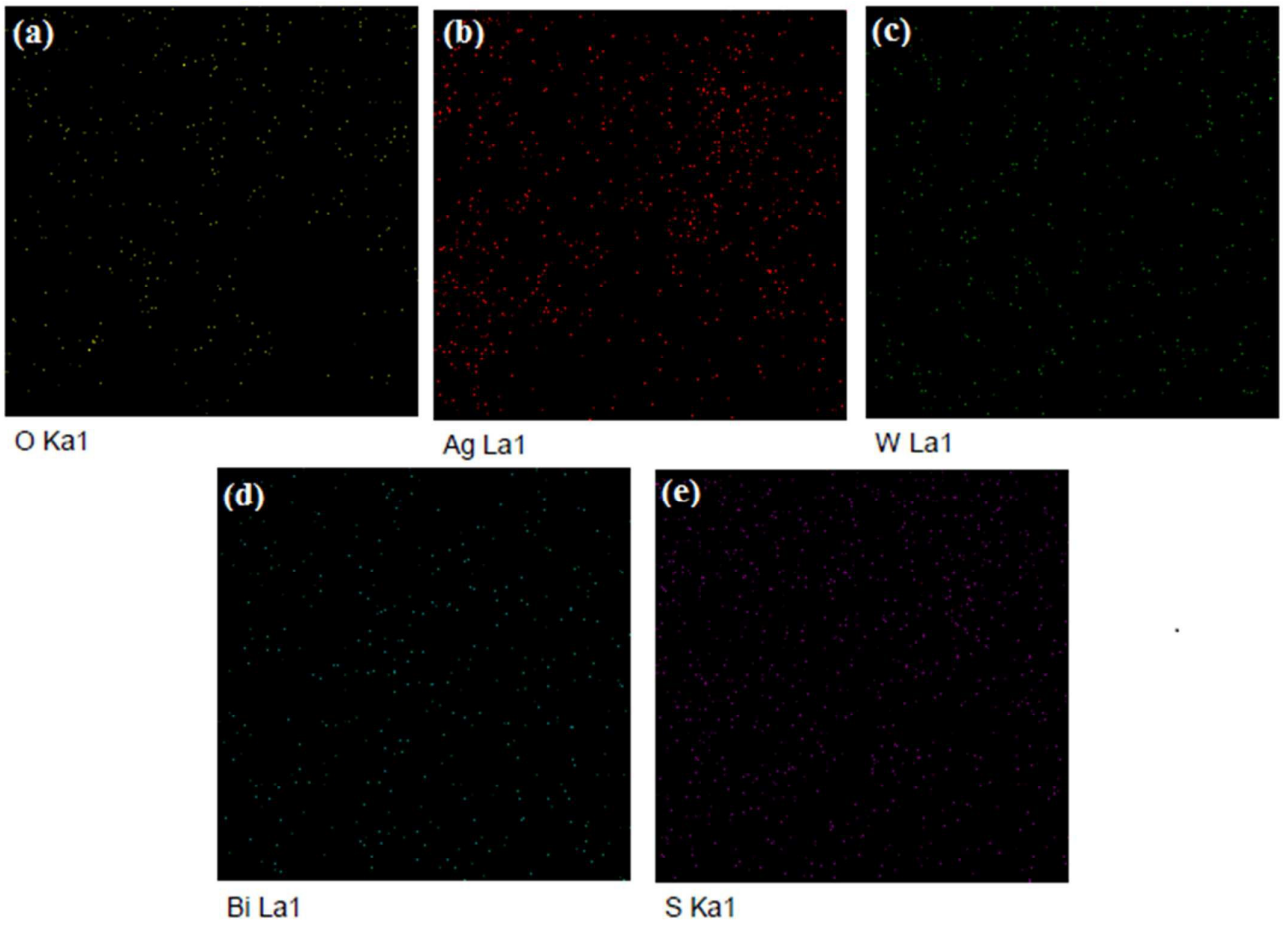

Fig.5

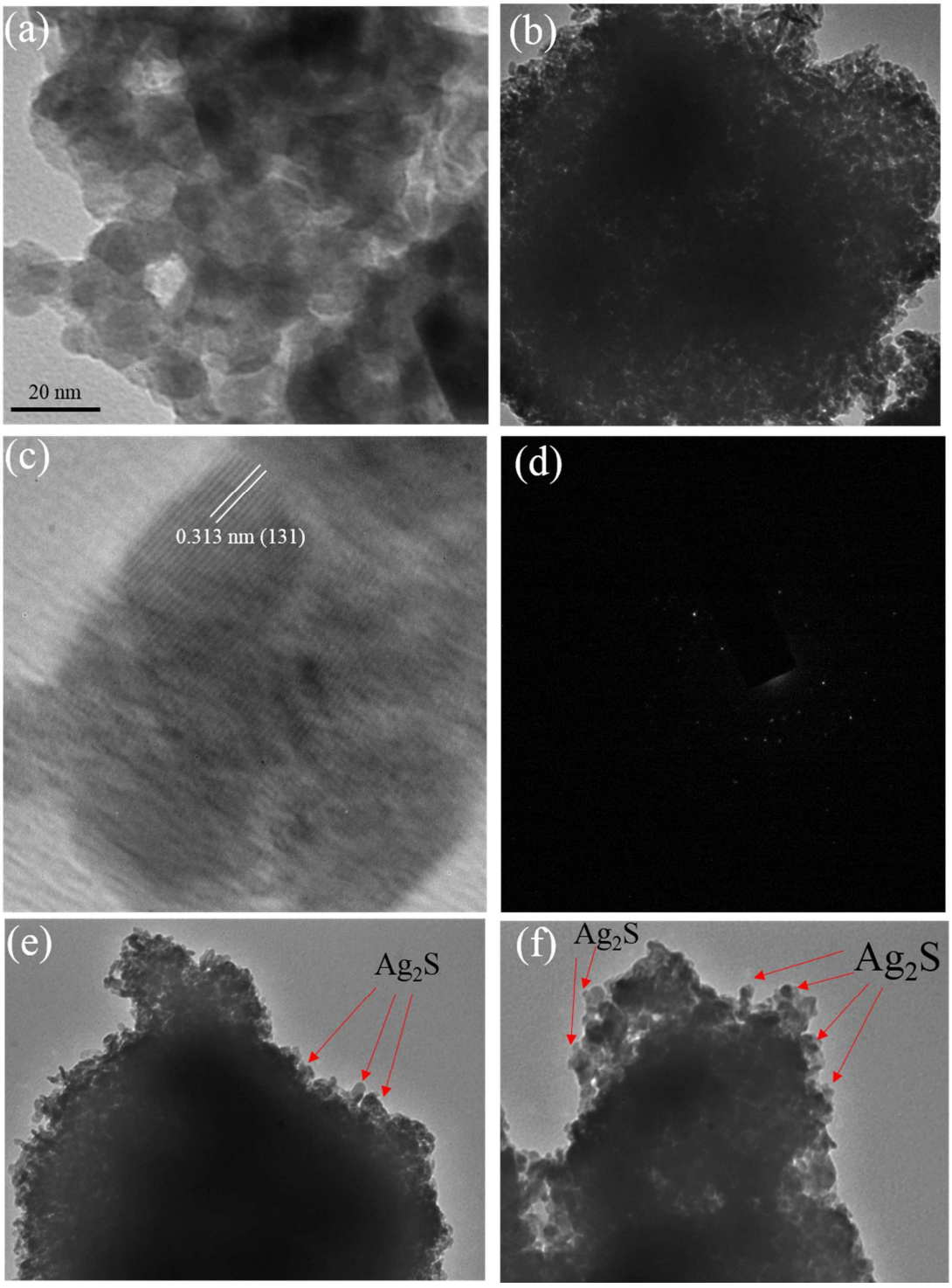

Fig.6

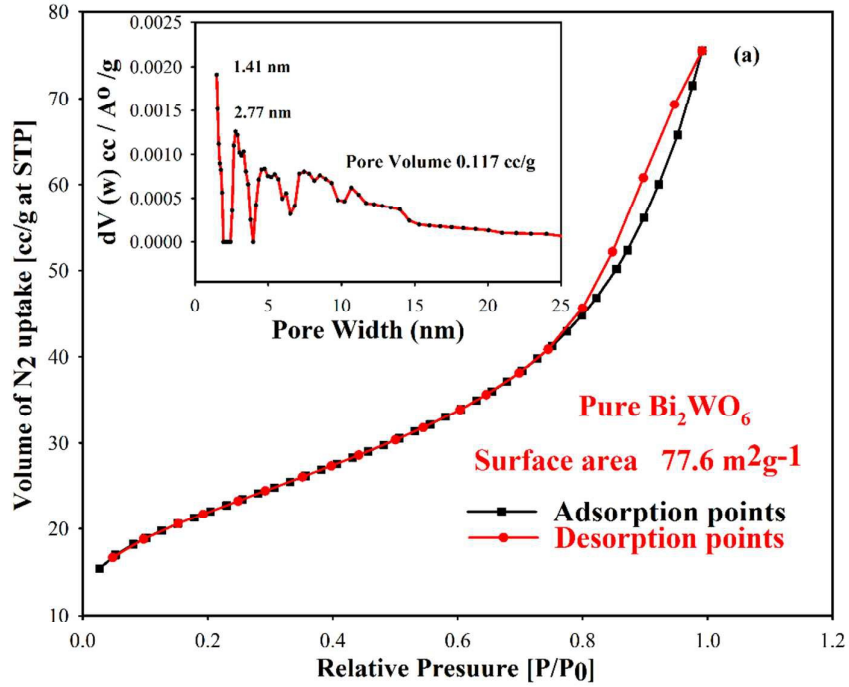

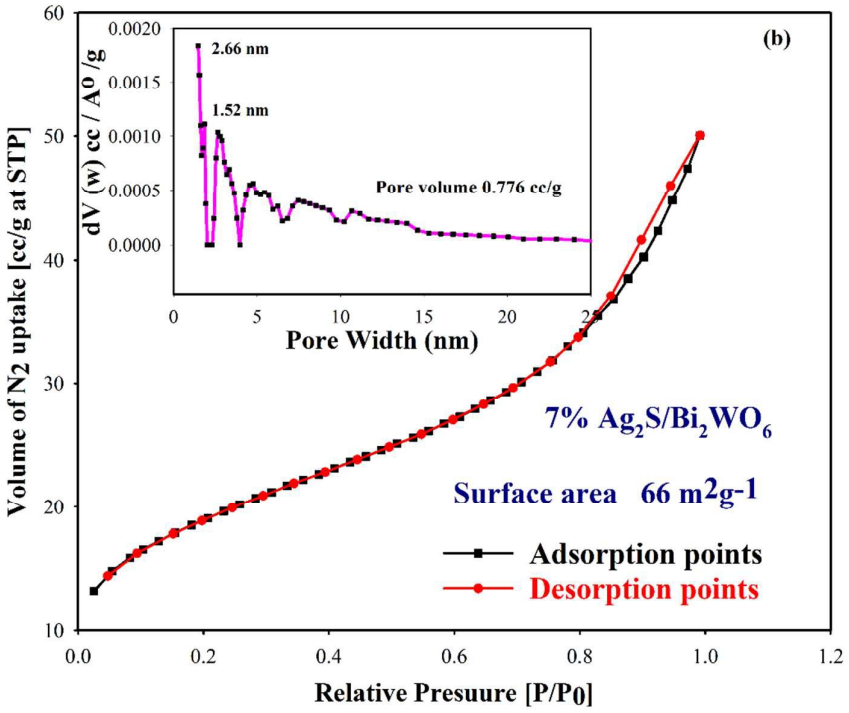

Fig. 7

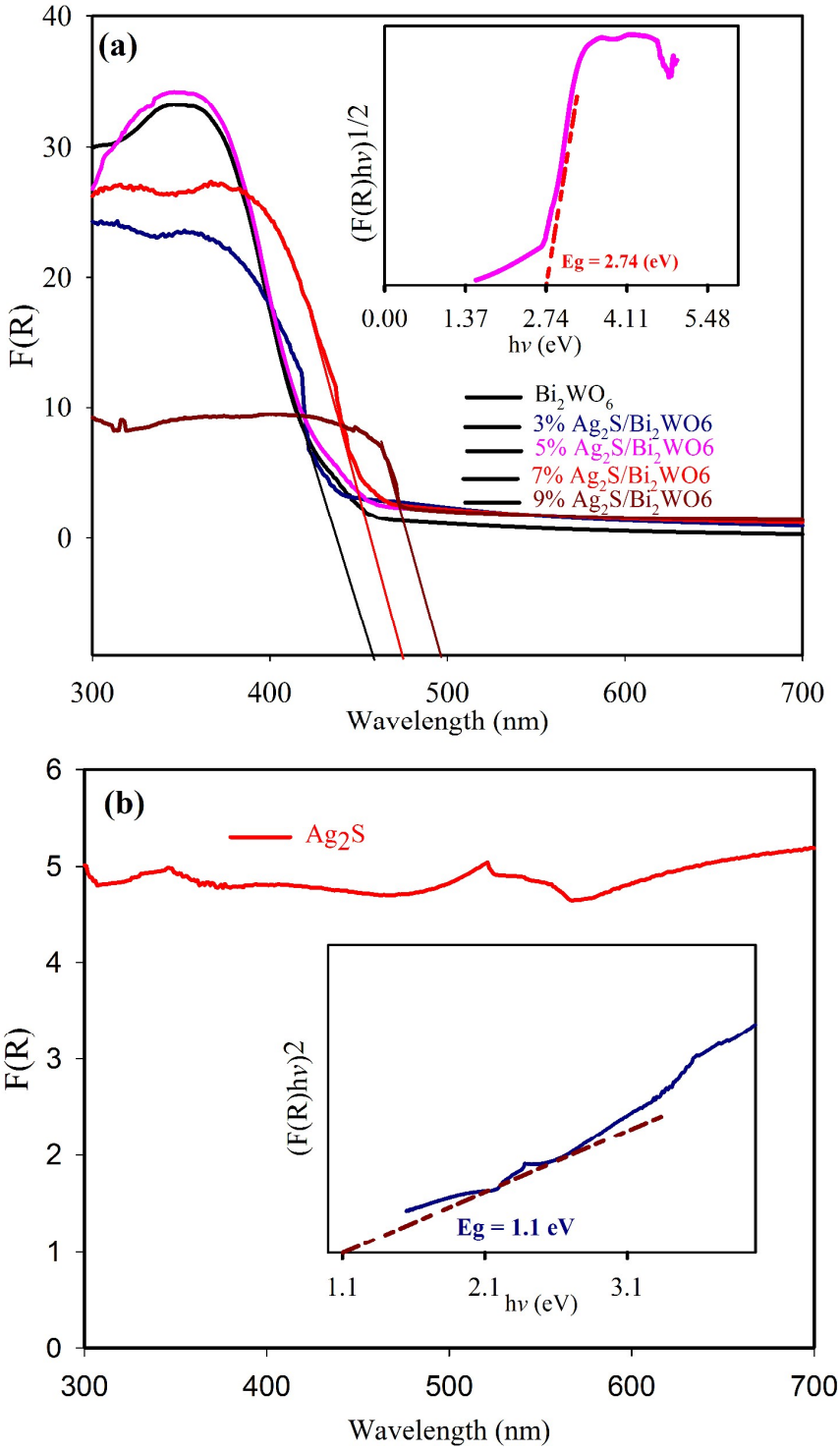

Fig. 8

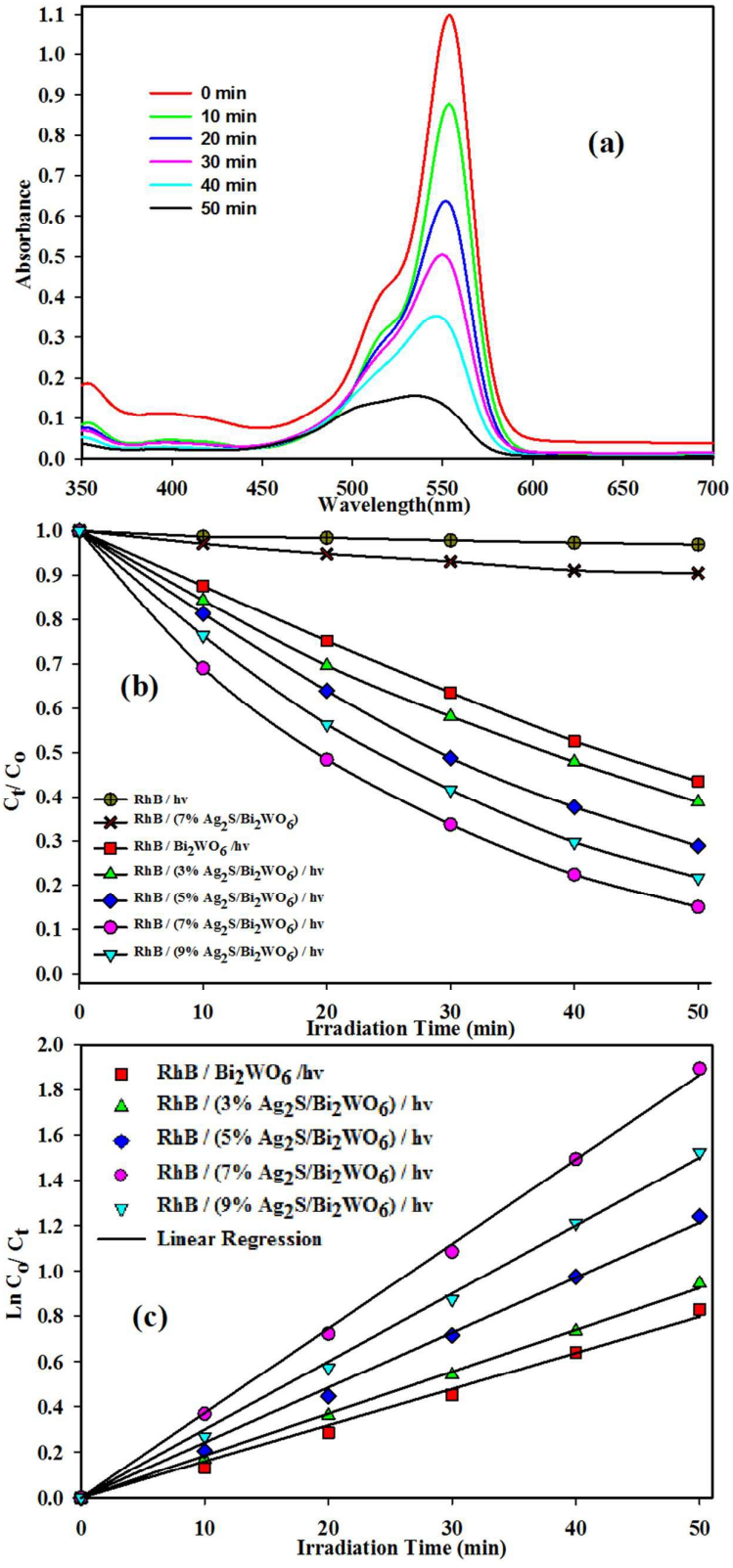

Fig. 9

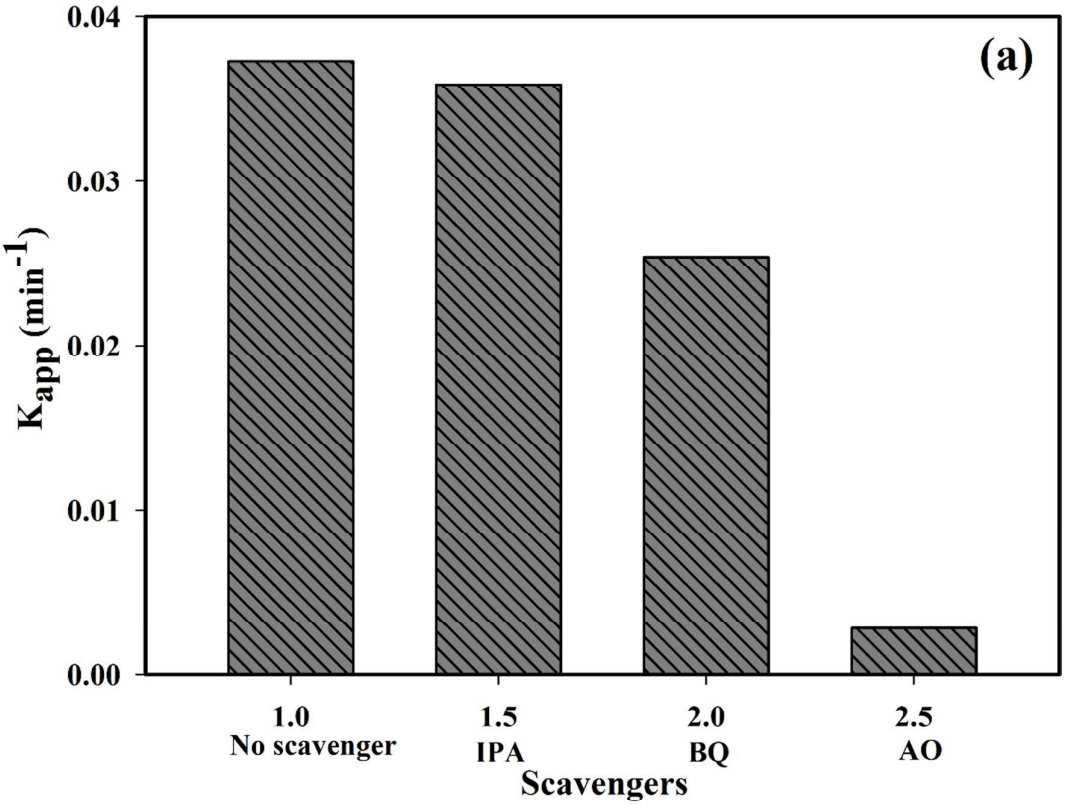

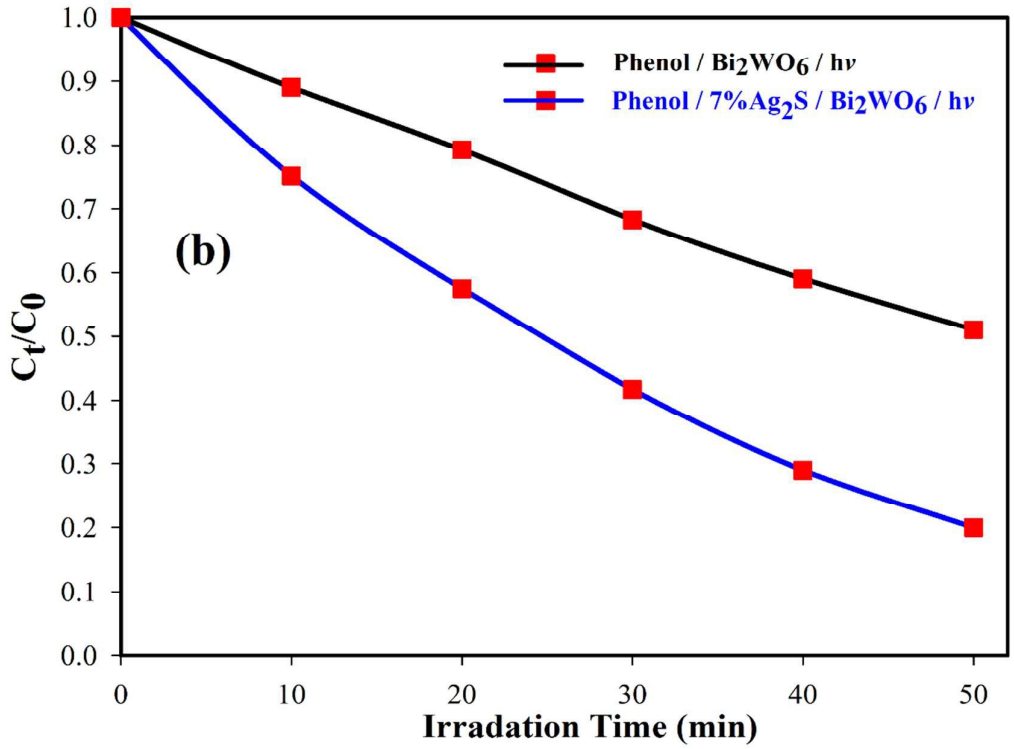

Fig. 10

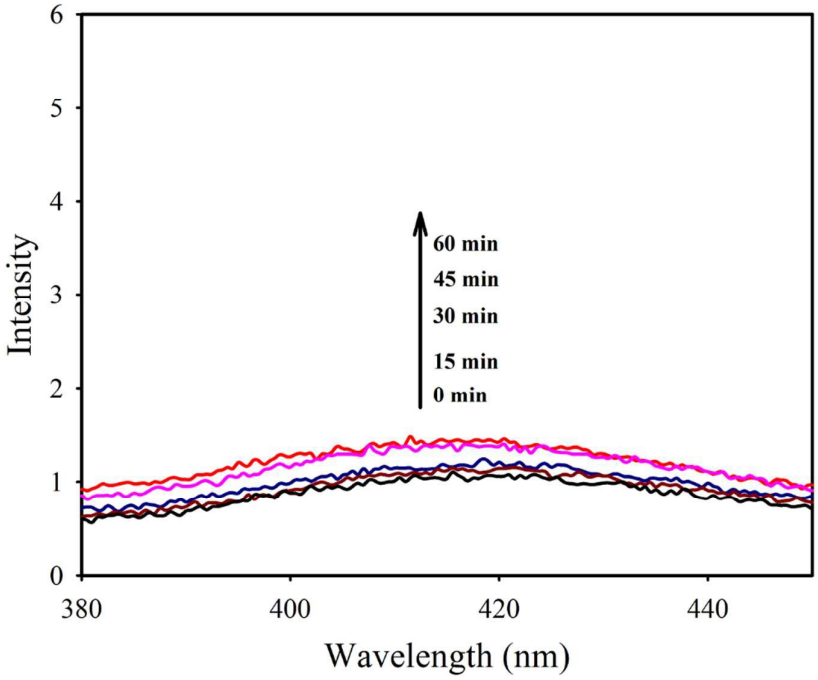

Fig.11

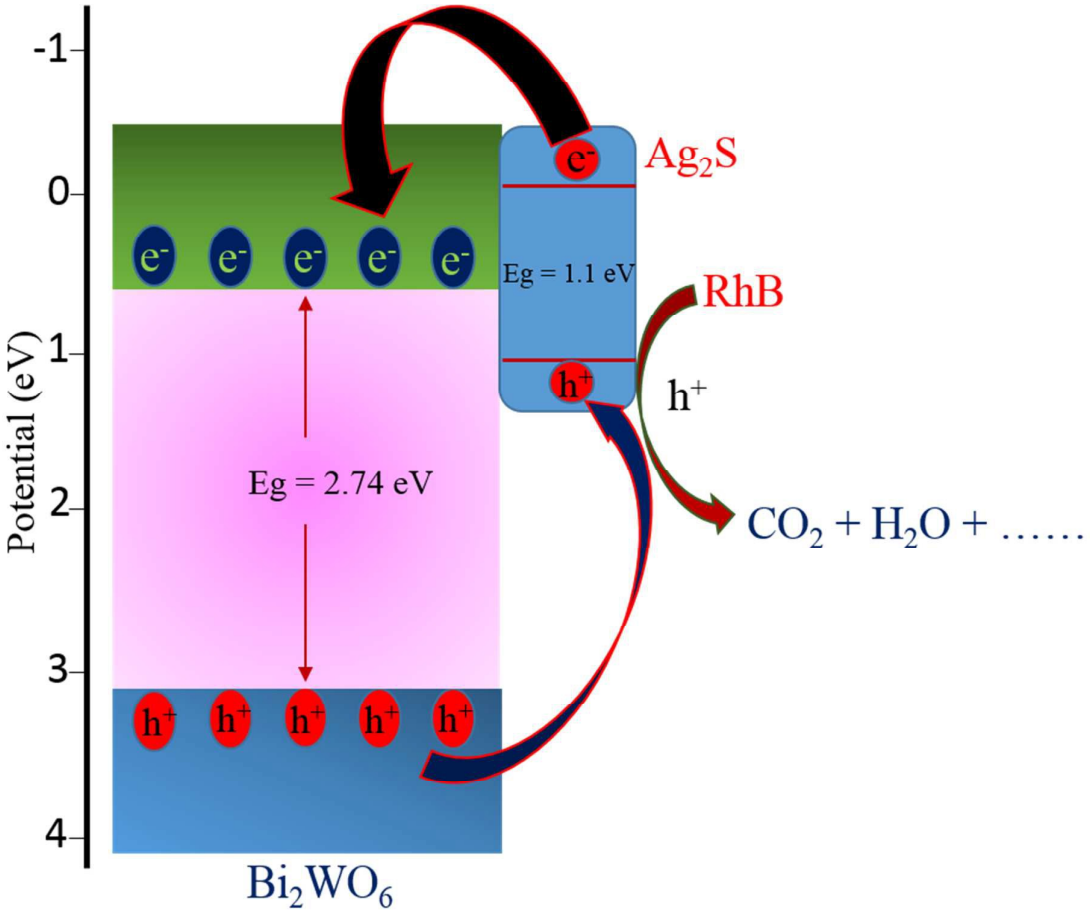

Fig. 12

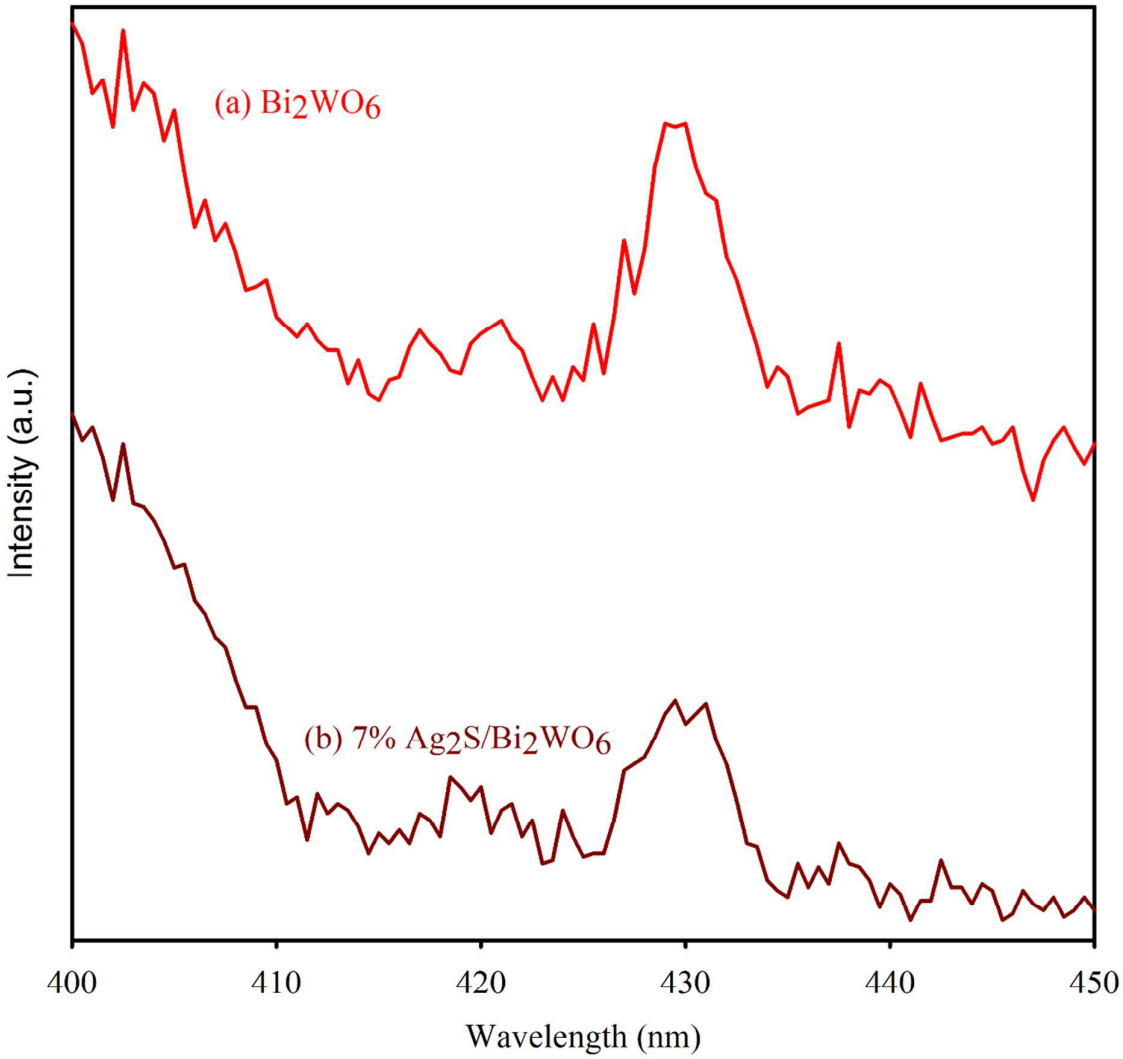

Fig. 13

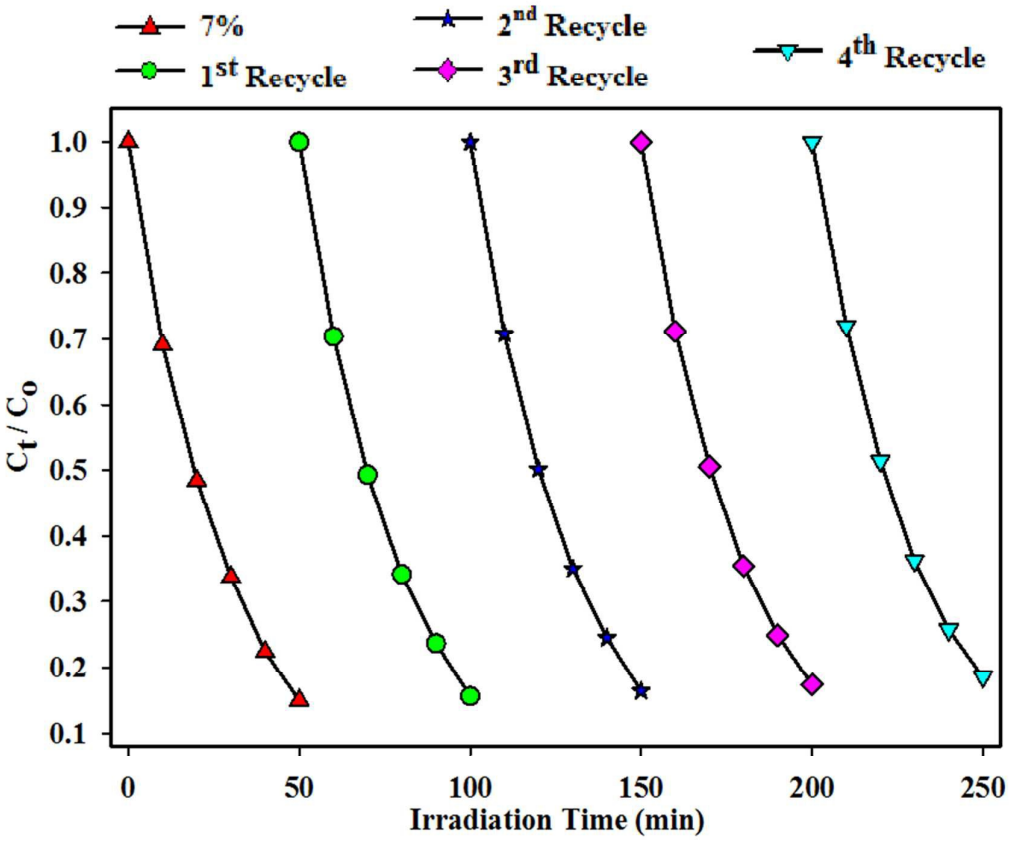

Fig. 14

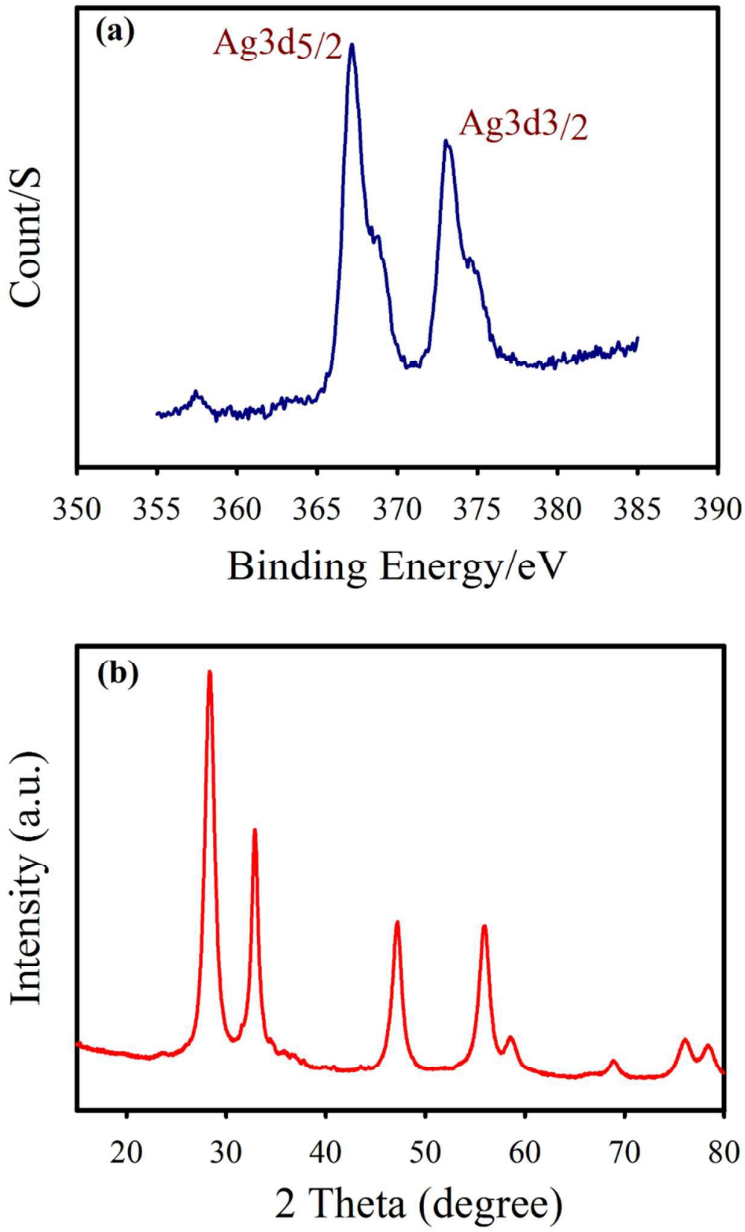

Table. 1

Pseudo-first-order rate constants (k_{app}) calculated from the plots of ln (C_0/C_t) versus irradiation time for decolorization of RhB over different catalysts, % decolorization of RhB and average crystallite size of Pure Bi_2WO_6 and Ag_2S/Bi_2WO_6 catalysts with different Ag_2S contents.

Sample	$K_{app}(min^{-1})$	% decolorization	Average Crystallite size (nm)
Bi_2WO_6	0.0160	56.42994	11.12
3% Ag_2S/Bi_2WO_6	0.0185	61.11649	11.28
5% Ag_2S/Bi_2WO_6	0.0243	71.10206	10.56
7% Ag_2S/Bi_2WO_6	0.0373	84.96666	10.66
9% Ag_2S/Bi_2WO_6	0.0300	78.2553	11.42

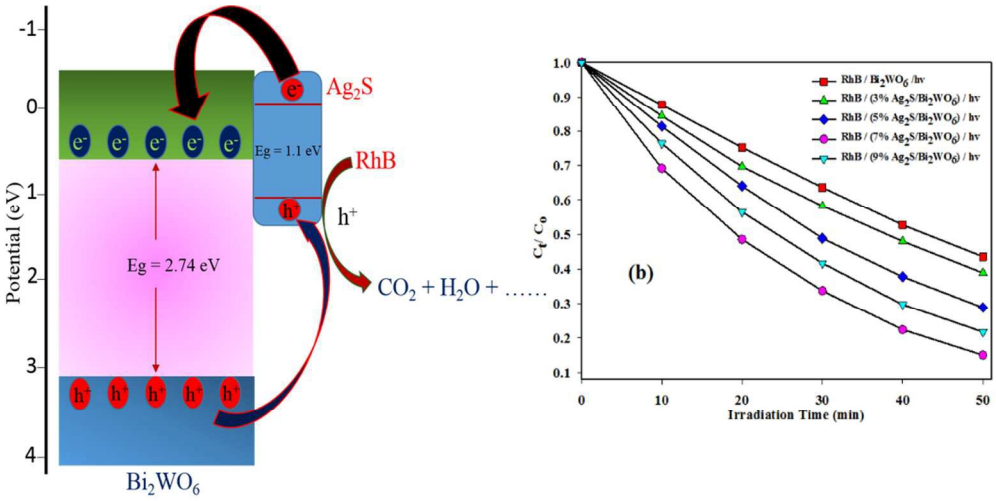

203x102mm (150 x 150 DPI)